Numerical simulation of two-dimensional late-stage coarsening for nucleation and growth

Norio Akaiwa and D. I. Meiron
Applied Mathematics, 217-50, California Institute of Technology, Pasadena, California 91125
(Received 30 November 1994)

Numerical simulations of two-dimensional late-stage coarsening for nucleation and growth or Ostwald ripening are performed at area fractions 0.05 to 0.4 using the monopole and dipole approximations of a boundary integral formulation for the steady state diffusion equation. The simulations are performed using two different initial spatial distributions. One is a random spatial distribution, and the other is a random spatial distribution with depletion zones around the particles. We characterize the spatial correlations of particles by the radial distribution function, the pair correlation functions, and the structure function. Although the initial spatial correlations are different, we find time-independent scaled correlation functions in the late-stage of coarsening. An important feature of the late-stage spatial correlations is that depletion zones exist around particles. A log-log plot of the structure function shows that the slope at small wave numbers is close to 4 and is -3 at very large wave numbers for all area fractions. At large wave numbers we observe oscillations in the structure function. We also confirm the cubic growth law of the average particle radius. The rate constant of the cubic growth law and the particle size distribution functions are also determined. We find qualitatively good agreement between experiments and the present simulations. In addition, the present results agree well with simulation results using the Cahn-Hilliard equation.

PACS number(s): 64.60.My, 64.60.Qb, 64.75.+g

I. INTRODUCTION

Late-stage phase separation of two phase mixtures has recently been studied through the use of numerical simulations in both two and three dimensions. Generally, phase separation is classified in two categories. One is spinodal decomposition in which the second phase domains have interconnected structure, and the other is nucleation and growth where the domains consist of isolated particles. The quench positions and the lattice structures of the majority and minority phases determine the domain structures. In the late stage of phase separation, both of the phenomena are driven by reduction in total surface area through diffusion, resulting in an increase of the average domain size. The late stage of nucleation and growth is known as coarsening or Ostwald ripening. Spinodal decomposition is generally studied using the Cahn-Hilliard (CH) model [1]. In this model the time evolution of the concentration field is governed by a nonlinear time-dependent diffusion equation. The CH model is also applicable to nucleation and growth when the free energy of the system can be represented by a single curve which in general is not the case for solid-solid or solid-liquid systems. In the late stage of nucleation and growth where the supersaturation is very small, a steady state linear diffusion equation may be a good approximation to the diffusion field. The advantage of the use of the steady state diffusion equation is that the formulation is much simpler than that of the CH model. In addition, this formulation does not depend on the free energy curves of the system.

In this paper, we study two-dimensional late-stage coarsening using the monopole and dipole approximations of a boundary integral formulation for the steady state diffusion equation. It is well known in three dimensions that the average particle radius $\langle r \rangle$ obeys a scaling form $\langle r \rangle^3 \sim t$, and that the particle size distribution becomes time independent when scaled by the average radius in the late stage. This was first derived by Lifshitz and Slyozov [2], and Wagner [3] (LSW). However, this theory is valid only in the limit of zero volume fraction. Many attempts have been made to extend the validity of the theory in three dimensions (see Ref. [4] and references cited therein).

In two dimensions, a mean field approach similar to that in LSW theory is not applicable since the general solution of the steady state diffusion equation diverges logarithmically at large distances. The first theoretical study in two dimensions was performed by Marqusee [5]. The average concentration field was approximated using a modified Helmholtz equation. Thus the divergence at large distances was removed due to the annihilation term in the Helmholtz equation. The cubic growth law and the existence of the time-independent scaled size distribution were found also in two dimensions. The same Helmholtz equation which was assumed in Marqusee's theory was derived by Hayakawa and Family [6] using the ring diagram approximation. Zheng and Gunton (ZG) [7] extended the method developed by Marder [8], in which the effects of particle correlations are taken into account, for two dimensions. As pointed out by these authors, this method is not applicable for area fractions larger than 0.01. Even at very small area fractions, the rate constant of the cubic growth law is much larger than the others. Ardell [9] extended his three-dimensional theory [10] to the two-dimensional case. In this mean field theory, the concentration at a certain distance from a par-

ticle, which is determined by a mean free distance of the nearest neighbors, is approximated by a constant. Yao, Elder, Guo, and Grant (YEGG) [11] added a source term in the Helmholtz equation. However, their theory is not applicable for area fractions larger than 0.085. All of the theories predict $\langle r \rangle^3 \sim t$, but with different rate constants and size distributions. It is unclear which theory describes the nature of the late-stage coarsening well.

Numerical simulations of two-dimensional coarsening for a small number of particles were first performed by Voorhees, McFadden, Boisvert, and Meiron [12] using the boundary integral method. The objective of the simulations was to test how particles change their shapes during coarsening at large area fractions. Similar simulations were performed by Imaeda and Kawasaki [13] using the multipole expansion method. Larger scale simulations were performed by Rogers and Desai [14], Chakrabarti, Toral, and Gunton (CTG) [15], and Lacasta, Sancho, Hernández-Machado, and Toral [16] using the CH equation with a Ginzburg-Landau form as a free energy functional. Küpper and Masbaum [17] performed simulations using a free energy functional determined by experimental data of a real alloy. Although these simulations give scaling results for area fractions larger than 0.2, the scaling behavior is not satisfactory at lower area fractions. The disadvantage of simulations using the CH equation is that the system size is restricted due to the speed and memory size of present day computers. Yao *et al.* [11] performed simulations using the monopole approximation and systems of 1000 initial particles. The simulations were performed at area fractions less than 0.1, and the systems do not seem to reach an asymptotic state, probably due to the small system size.

Recent work in coarsening has concentrated on the spatial correlations of particles created by the long time diffusional interactions. The importance of the spatial correlations has been pointed out by Marder [8] and Tokuyama and Kawasaki [18]. However, due to the complicated many body effects, present theoretical understanding of these correlations is not satisfactory.

The objective of this paper is to perform numerical simulations using much larger systems than those used previously. We investigate the particle spatial correlations in both real and Fourier spaces through the use of the radial distribution function, the pair correlation functions, and the structure function. We also determine the particle size distribution function and the rate constant of the growth law. Finally, the results are compared with experiments, theories, and other simulations.

II. NUMERICAL SIMULATION

We consider a system which consists of N circular minority phase particles. Note that all variables used in this section are nondimensionalized (see Ref. [4] for scaling). The dimensionless concentration u in the matrix phase satisfies the steady state diffusion equation:

$$\nabla^2 u = 0. \tag{2.1}$$

In the late stage, the supersaturation is very small compared with the concentration difference between the majority and minority phases. Thus it is expected that the diffusional time scale is much smaller than the time scale for interfacial motion. This is the justification of the validity of Eq. (2.1). The boundary condition on the surface of each particle is given by the Gibbs-Thomson equation

$$u(\mathbf{p}) = \frac{1}{r_j} \quad \text{for } \mathbf{p} \text{ on } S_j, \tag{2.2}$$

where $\mathbf{p}$ is the position vector of the point p, r_j is the radius and S_j is the surface of particle j, respectively. Mass is conserved in the system so that the summation of the normal derivative of the concentration at particle surfaces is zero:

$$\sum_{j=1}^{N} \int_{S_j} \sigma(\mathbf{p}) dS_j = 0, \tag{2.3}$$

where

$$\sigma(\mathbf{p}) = \frac{\partial u(\mathbf{p})}{\partial n_p}, \tag{2.4}$$

and the normal vector $\mathbf{n}_p$ is directed outward from the particle. The flux conservation condition at each point on the interface of a particle is given by

$$v_n(\mathbf{p}) = \frac{\partial u(\mathbf{p})}{\partial n_p} = \sigma(\mathbf{p}), \tag{2.5}$$

where v_n is the normal velocity of the interface.

Since the concentration is constant on the surface of each particle, the integral form of Eq. (2.1) is given by [4]

$$u(\mathbf{p}) = \frac{1}{2\pi} \sum_{j=1}^{N} \int_{S_j} \sigma(\mathbf{q}) g(\mathbf{p}, \mathbf{q}) \mathbf{dq} + u_0, \tag{2.6}$$

where

$$g(\mathbf{p}, \mathbf{q}) = \ln |\mathbf{p} - \mathbf{q}|, \tag{2.7}$$

and u_0 is a constant which accounts for the contribution from the external boundary. Equation (2.6) has a unique solution, so $\sigma(\mathbf{q})$ can be evaluated by solving Eq. (2.6) with the boundary condition Eq. (2.2) and the mass conservation condition Eq. (2.3).

We expand $\sigma(\mathbf{p})$ in a Fourier series:

$$\sigma(\mathbf{p}) = \frac{1}{2} A_0^{(j)} + \sum_{n=1}^{\infty} (A_n^{(j)} \cos n\theta_{\mathbf{r}_j} + B_n^{(j)} \sin n\theta_{\mathbf{r}_j})$$

$$\text{for } \mathbf{p} \text{ on } S_j,\ j = 1, 2, \ldots, N, \tag{2.8}$$

where $\mathbf{r}_j$ is a vector locating a point on the surface of particle j with its origin at the center of particle j, and $A_n^{(j)}$ and $B_n^{(j)}$ are constants to be determined. Note that $B_0^{(j)} = 0$. Performing the integrals in Eqs. (2.3) and (2.6) (see Appendix) and using the boundary condition, Eq. (2.2), we obtain

$$A_n^{(j)} = -\sum_{\substack{k=1\\k\neq j}}^{N}\sum_{m=0}^{\infty}(-1)^m \binom{n+m-1}{m} \frac{r_j^{n-1} r_k^{m+1}}{d_{jk}^{n+m}} \times\left\{A_m^{(k)}\cos[(n+m)\theta_{d_{jk}}] + B_m^{(k)}\sin[(n+m)\theta_{d_{jk}}]\right\} \quad (n\neq 0), \tag{2.9}$$

$$B_n^{(j)} = -\sum_{\substack{k=1\\k\neq j}}^{N}\sum_{m=0}^{\infty}(-1)^m \binom{n+m-1}{m} \frac{r_j^{n-1} r_k^{m+1}}{d_{jk}^{n+m}} \times\left\{A_m^{(k)}\cos[(n+m)\theta_{d_{jk}}] - B_m^{(k)}\sin[(n+m)\theta_{d_{jk}}]\right\} \quad (n\neq 0), \tag{2.10}$$

$$\frac{1}{r_j} = \frac{1}{2}A_0^{(j)} r_j \ln r_j + u_0 + \sum_{\substack{k=1\\k\neq j}}^{N}\frac{1}{2}A_0^{(k)} r_k \ln d_{jk} + \sum_{\substack{k=1\\k\neq j}}^{N}\sum_{n=1}^{\infty}\frac{(-1)^{n-1} r_k^{n+1}}{2n d_{jk}^n} \times\left[A_n^{(k)}\cos(n\theta_{d_{jk}}) + B_n^{(k)}\sin(n\theta_{d_{jk}})\right], \tag{2.11}$$

$$\sum_{j=1}^{N} r_j A_0^{(j)} = 0, \tag{2.12}$$

where d_{jk} is a separation distance between the centers of particles j and k. Thus Eqs. (2.9) – (2.12) yield a $[(2n_c+1)N+1]\times[(2n_c+1)N+1]$ set of linear equations for the coefficients $A_n^{(j)}$, $B_n^{(j)}$, and u_0, where n_c is a truncation of the expansion.

Since we have assumed that the particles are circular, the expansion is truncated at $n_c = 0$, the monopole approximation (referred to as M), and $n_c = 1$, the dipole approximation (referred to as D). The monopole term corresponds to the areal growth rate of the particle:

$$\frac{da_j}{dt} = \pi r_j A_0^{(j)}, \tag{2.13}$$

where a_j is the area of particle j. The dipole terms correspond to the translation velocity of the center of the particle:

$$\frac{d\mathbf{R}_j}{dt} = (A_1^{(j)}, B_1^{(j)}), \tag{2.14}$$

where $\mathbf{R}_j$ is the position vector of the center of particle j. Note that the particles remain circular if the expansion is truncated at the dipole level. If higher order terms are included, the particles change their shapes. Since this violates our constraint of circular shape, we do not include the higher order terms. Experiments [19] and simulations using the CH equation [14,15] show that all particles are almost circular if the area fraction of the minority phase is smaller than about 0.3. When the separation distances between particles are small, the monopole and dipole approximations give poor results. However, as will be shown later, the particles are well separated in the late stage. Thus we believe that both monopole and dipole approximations are valid at small area fractions. The validity of these approximations will be discussed later.

We perform simulations at area fractions, $\phi = 0.05$, 0.13, 0.2, 0.3, and 0.4. The monopole approximation is employed at $\phi = 0.05$, 0.13, and 0.2 and the dipole approximation is employed at higher area fractions. At $\phi = 0.13$ and 0.2, we also perform simulations using the dipole approximation. Four independent runs are performed for each area fraction, and the results shown in the following section are the averages of these runs.

As mentioned earlier, the system size must be very large to allow the system to reach the asymptotic state. Basically, an $(N+1)\times(N+1)$ linear system of equations has to be solved to determine the growth rate of the particles if the monopole approximation is employed. Although the diffusion propagator $\ln|\mathbf{p}-\mathbf{q}|$ diverges as $|\mathbf{p}-\mathbf{q}|\to\infty$, the diffusion field is screened due to the mass conservation constraint. Thus we only need to solve much smaller linear systems of equations. When the growth rate and the translation velocity of a particle are calculated, the effects of other particles separated far from the particle can be neglected [4]. The growth rate and the translation velocity are therefore calculated by neglecting the effects of particles separated by a certain cutoff distance. As this cutoff distance increases, the growth rate and the translation velocity asymptotically approach constant values. Figure 1 shows the absolute value of the error in the growth rate A_0 using the monopole approximation relative to the asymptotic value $A_0(\infty)$ as a function of the cutoff distance x_c at $\phi = 0.13$. The results of ten different configurations are shown in the figure. As the cutoff distance increases, the error decreases exponentially. Note that the error becomes smaller than machine precision at $x_c/\langle r\rangle$ larger than 60. Thus A_0 at the largest x_c was used as the asymptotic

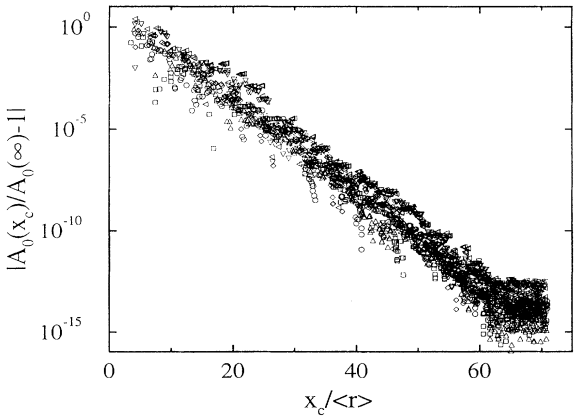

FIG. 1. The absolute value of the error in the growth rate using the monopole approximation relative to the asymptotic value $A_0(\infty)$ as a function of the cutoff distance at $\phi = 0.13$.

value. We performed smaller scale simulations using different values of the cutoff distance to determine the proper value. If the cutoff distance is large enough, the choice of the cutoff distance does not affect the final results. The cutoff distances scaled by the average radius used in the simulations and the average number of particles in the interaction range, N_c, are listed in Table I. Thus we need to solve $[N_c(2n_c+1)+1]\times[N_c(2n_c+1)+1]$ linear systems of equations N times for each time step. The computational cost for each time step is then proportional to N rather than N^3, and N_c determines the precision. Note that the computational cost of the dipole approximation is about 27 times larger than that of the monopole approximation. Using the cutoff distances shown in Table I, relative errors of the growth rate and the translation velocity with the asymptotic values are much better than 0.5% for most cases. If the growth rate A_0 is close to 0, the error is bigger but does not exceed 1%. When a particle is located near the edge of the computational cell, periodic images of other particles are used to avoid the effects of finite system size.

The area of particles is updated by

$$a_j(t+\Delta t) = a_j(t) + \pi r_j A_0^j \Delta t. \tag{2.15}$$

Since we expect that $\langle r\rangle^3$ is proportional to t, Δt is chosen as

$$\Delta t = \frac{\langle r\rangle^3}{\langle r_0\rangle^3}\tau\ , \tag{2.16}$$

where $\langle r_0\rangle$ is the average radius at $t=0$ and τ is a constant. We chose $\tau = 0.005$ for all cases except for $\phi = 0.4$. For $\phi = 0.4$, $\tau = 0.0035$ was used. Using this method the area of particles can become negative if the radius of the particle is small and τ is large. This results in an increase of the area fraction since the total mass is conserved in the system. To avoid this area fraction change, particles smaller than $0.1\langle r\rangle$ are removed from the system before calculating the growth rate and the translation velocity. As mentioned earlier, the present model is based on the approximation that the diffusional time scale is much smaller than the time scale for the interfacial motion. We note, however, that for very small particles, the time scale for the interfacial motion is comparable to the diffusional time scale. In addition, the Gibbs-Thomson equation may not be valid in this regime since curvatures are large. Thus the formulation is no longer valid for such particles. A small particle disappears by giving its mass to surrounding particles. The change of area of the surrounding particles due to the mass from the small particle may be very small if the removal radius is small enough. Since the rate of shrinkage of the small particle is very large, the time required to diffuse this particle into the matrix phase is very small compared with Δt. Thus it is expected that the change of area of the surrounding particles during the time interval Δt is not greatly affected by the removed particle. Simulations using the smaller τ and removal radius were performed, and we did not find any significant differences. Thus it is expected that particle removal does not yield serious errors. In all cases, the area fraction increase was smaller than 2% at the end of the simulations.

TABLE I. The cutoff distance $x_c/\langle r\rangle$, the average number of particles in the interaction range, N_c, and the constant d_ϕ.

ϕ	$x_c/\langle r\rangle$	N_c	d_ϕ
0.05	37.0	65	2.5
0.13	19.0	45	1.15
0.2	14.0	38	0.74
0.3	10.5	31	0.44
0.4	9.0	30	0.23

We employ 100 000 particles initially. Two methods are used to place the particles in the computational cell. The first method is to place a set of particles with the size distribution function determined from simulations with fewer particles randomly without overlaps. The second approach is to use the same initial size distribution, but each particle has a depletion zone from which particles are excluded. Thus each particle has the excluded area of a circular shell of thickness $r_j d$ where d is a constant. The constants used at each area fraction, d_ϕ, are also listed in Table I. Both methods generate different spatial correlations. As will be shown later, both of the initial spatial correlations are much different from the asymptotic spatial correlations in the late stage. At $\phi = 0.05$, 0.13, and 0.2, simulations are performed using the initial distributions without depletion zones, $d = 0$, and with depletion zones $d = d_\phi$ listed in Table I. We only perform simulations using the initial distribution with $d = d_\phi$ at $\phi = 0.3$ and 0.4. This is because a large number of particles overlap in the initial and intermediate stages if an initial distribution with $d = 0$ is employed. In this case, the area fraction increase is very large and the particle size distribution has a long tail at large radii due to the error introduced by the overlaps.

Most of the computational time is spent in creating the asymptotic spatial correlations. Our purpose is to determine the asymptotic correlation functions in the late stage, so the time evolution of the spatial correlations is not important. In addition, both of the initial spatial correlations may be different from the spatial correlations created during the nucleation stage in real systems. Thus a smaller cutoff distance, $0.5x_c$, and a larger time increment, 2τ, are used until the number of particles decreases to 20 000. At the end of the rough simulation, we found about 2% increase of the area fraction and some overlapping particles. The area fraction and particle overlaps are adjusted by slightly changing the radius and location of particles. This particle configuration is used as a new initial condition for a fine simulation. At this time, the scaled spatial correlation functions are much closer to the asymptotic correlation functions in the late stage than those of the initial distributions. However, the scaled correlation functions are still time dependent. The simulations are then continued until the number of particles becomes 100.

The disadvantage of the monopole and dipole approximations is that the particles can overlap. This is because interfacial deformation is not allowed in the simulations.

If simulations are performed without the shape restriction, the particles do not overlap [12,13]. We found some overlaps in the initial and intermediate stages. The worst case is the simulation at $\phi = 0.2$ using the monopole approximation and $d = 0$. In the initial stage, about 1% of particles are overlapping, but the number of overlapping particles decreases as time increases. We did not find any overlaps in the late stage for all area fractions.

III. RESULTS AND DISCUSSION

It is expected that the cube of the average particle radius is proportional to time in the late stage so that

$$\langle r \rangle^3 = Kt + C \tag{3.1}$$

holds, where K is the rate constant and C is an effective offset. In order to see this behavior, a log-log plot of average radius versus time is displayed in Fig. 2. The solid line in the figure indicates the slope of 1/3. The results using the monopole approximation without initial depletion zones, $d = 0$, and with initial depletion zones, $d = 1.15$, at $\phi = 0.13$ are shown. The average radius and time are scaled by $1/\langle r_0 \rangle$, and $1/\langle r_0 \rangle^3$, respectively, in the figure. Note that $t = 0$ corresponds to the beginning of the fine simulation and $\langle r_0 \rangle$ is the average radius at this time. In the intermediate stage, $t = 1$–100, the results using two different initial conditions are slightly different. This is due to the different initial spatial correlations. The slopes n in the log-log plot determined by linear regression of the data points $t > t_c$ are listed in Table II. The values in the table are very close to 1/3 for all cases. Thus we believe that Eq. (3.1) holds in the late stage.

A. Radial distribution and pair correlation functions

The spatial correlations of particles in real space can be characterized by the radial distribution function and the pair correlation functions. We define the radial distribution function $G(x)$ as the ratio of the number of particles in a circular shell of radius x and thickness dx which surrounds a particle to the number of particles in the shell expected from the number density of the system [4]. The pair correlation function $G(r, r', x)$ is defined as the ratio of the number of particles of radius r' in the shell surrounding a particle of radius r to that expected from the number density. In order to obtain good statistics in the pair correlation functions, we divided the particles in two classes, larger than the average radius (L) and smaller than the average radius (S).

Figure 3 shows the radial distribution functions in the late stage and for random initial distributions with and without depletion zones at $\phi = 0.13$. The late time results are the averages of five different times after $t = 200$. While the radial distribution functions are time dependent at earlier times, we did not observe any time dependence after $t = 200$. The number of particles remaining in the system is about 900 at $t = 200$ corresponding to 0.9% of the initial number of particles. Although the initial radial distributions are different, the long time results evolve to a unique time-independent form. The late time results fall between the radial distribution functions of the two random spatial distributions. Note that the radial distribution functions for random initial dis-

TABLE II. The exponents of the growth law, n, in the late stage $t > t_c$.

ϕ	Approximation	n	t_c
0.05	M	0.330 ± 0.008	400
0.13	M	0.326 ± 0.003	200
	D	0.327 ± 0.001	200
0.2	M	0.332 ± 0.004	200
	D	0.331 ± 0.005	200
0.3	D	0.334 ± 0.005	100
0.4	D	0.326 ± 0.007	100

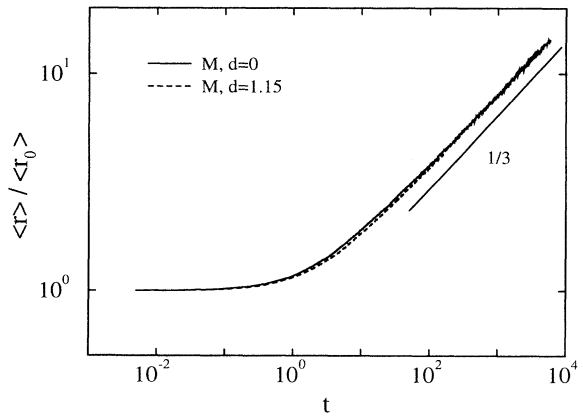

FIG. 2. A log-log plot of the average particle radius versus time at $\phi = 0.13$.

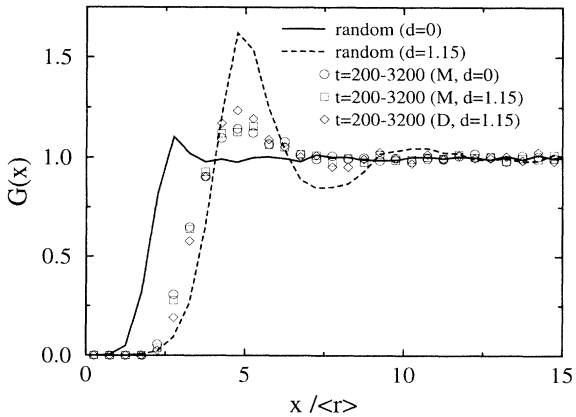

FIG. 3. The radial distribution functions in the late stage at $\phi = 0.13$. The radial distributions for the random distributions with $d = 0$ and 1.15 are also plotted.

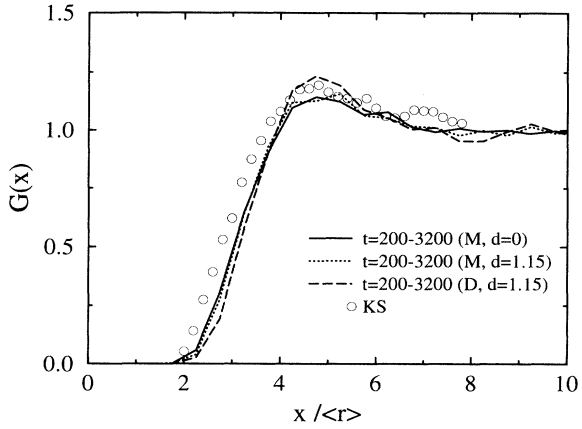

FIG. 4. Comparison of the radial distribution functions in the late stage and the experimental results by KS [19] at $\phi = 0.13$.

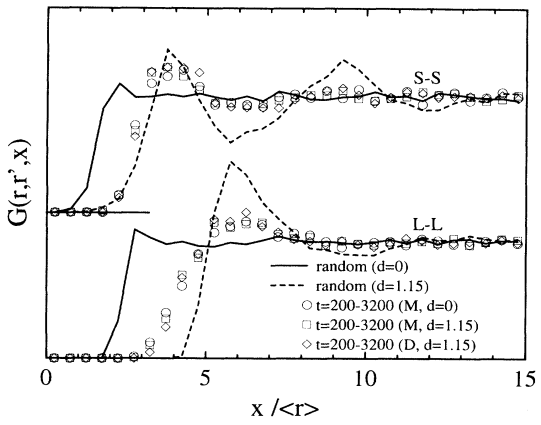

FIG. 6. The small-small and large-large correlation functions in the late stage at $\phi = 0.13$. The pair correlation functions for random distributions with $d = 0$ and 1.15 are also plotted.

tributions shown in the figure are calculated using the same particle size distribution as that in the late stage. We used the initial particle size distribution function obtained by simulations using fewer particles. This particle size distribution function is the same as that obtained for the late time results. Thus the differences in the radial distribution functions are purely due to the differences in the spatial correlations. An important feature in this figure is that depletion zones can be observed in the late stage. The number density of particles is smaller than that of the random distribution with $d = 0$ at small x. The radial distribution function with $d = 1.15$ approaches 1 in an oscillatory manner as $x/\langle r \rangle$ increases. However, this oscillatory behavior disappears in the late time results.

Figure 4 compares the radial distribution functions in the late stage and experimental results by Krichevsky and Stavans (KS) [19] at $\phi = 0.13$. The KS experiments were performed for succinonitrile in the liquid-solid coexistence region. The size of the particles is much larger than the sample thickness, so the system is effectively two dimensional. We found very good agreement between the results of KS and the present results. Figure 5 shows the small-large (S-L) correlation functions in the late stage and the KS results at $\phi = 0.13$. Note that the small-large and large-small correlation functions are identical. The present results in the late stage and the KS results agree reasonably well. The radial distribution function and the pair correlation functions depend not only on the particle spatial correlations but also on the particle size distribution function. As will be shown later, the agreement between the particle size distributions of the present results and the KS results is also reasonably good. Thus we believe that the qualitative features of the

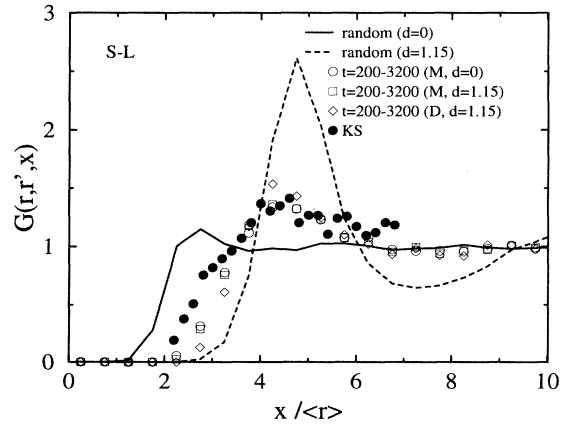

FIG. 5. Comparison of the small-large correlation functions in the late stage and the experimental results by KS [19] at $\phi = 0.13$. The pair correlation functions for random distributions with $d = 0$ and 1.15 are also plotted.

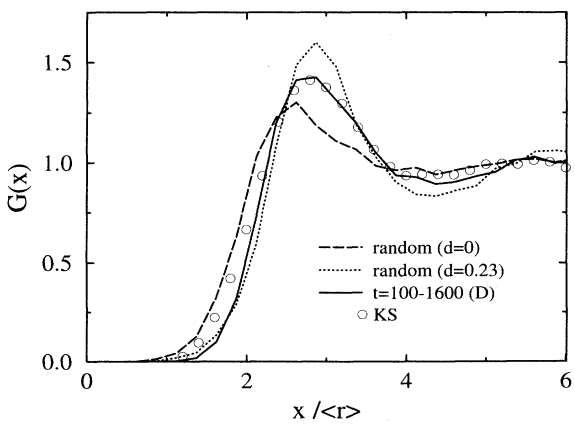

FIG. 7. Comparison of the radial distribution functions in the late stage and the experimental results by KS [19] at $\phi = 0.4$. The radial distributions for the random distributions with $d = 0$ and 0.23 are also plotted.

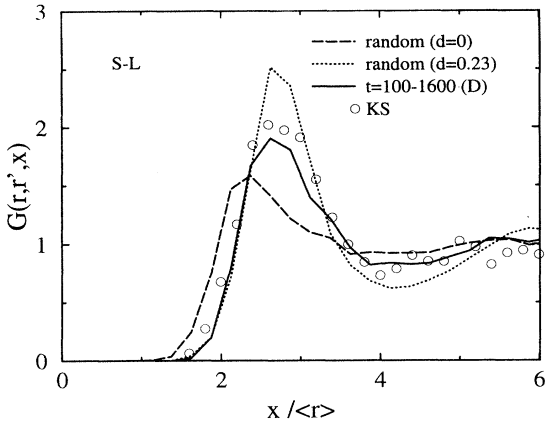

FIG. 8. Comparison of the small-large correlation functions in the late stage and the experimental results by KS [19] at $\phi = 0.4$. The pair correlation functions for random distributions with $d = 0$ and 0.23 are also plotted.

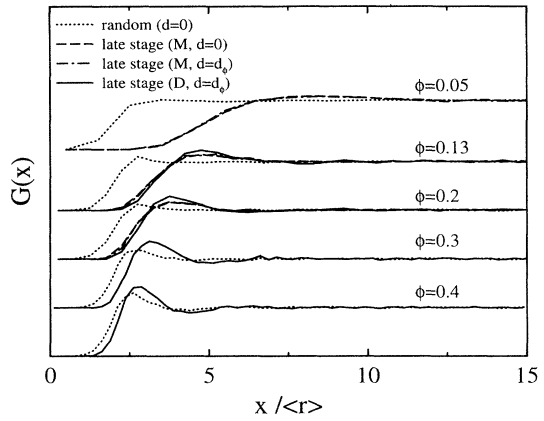

FIG. 10. The radial distribution functions in the late stage for various values of ϕ. The radial distributions for the random distributions with $d = 0$ are also plotted for reference.

spatial correlations in the late stage are well described in the present simulations.

The small-small (S-S) and large-large (L-L) correlation functions at $\phi = 0.13$ in the late stage are shown in Fig. 6. The correlation functions for random distributions are also plotted in the figure. For both cases, the late time results fall between the pair correlation functions for random distributions. We should emphasize that depletion zones exist in all pair correlation functions. This is the main feature of the spatial correlations in the late stage. We tried to reproduce the spatial correlation functions in the late stage by placing particles in the cell using different values of d. It is possible to obtain a good fit to the late-stage radial distribution function by carefully choosing d. However, this method does not yield the correct pair correlation functions.

Figures 7–9 show the radial distribution functions, the

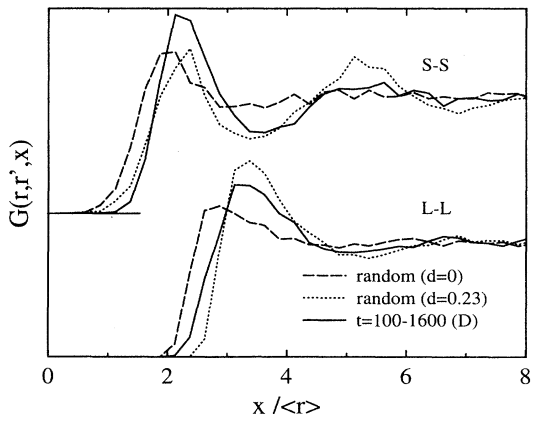

FIG. 9. The small-small and large-large correlation functions in the late stage at $\phi = 0.4$. The pair correlation functions for random distributions with $d = 0$ and 0.23 are also plotted.

S-L correlation functions, and the S-S and L-L correlation functions, respectively, at $\phi = 0.4$ in the late stage and for random distributions with $d = 0$ and 0.23. The results shown are the averages of five different times after $t = 100$. The KS results are also plotted in Figs. 7 and 8. The agreement between the late time results and the experiments is again quite good. We found that the qualitative features of the correlation functions at this area fraction are the same as those at $\phi = 0.13$.

It has been suggested that the small particles tend to be located near the large particles [8]. This conclusion was also reached by KS since there is a strong peak in the S-L correlation functions at small $x/\langle r\rangle$. We also observed such peaks in the S-L correlation functions. However, there exists a peak in all pair correlation functions at small $x/\langle r\rangle$ as shown in Figs. 5, 6, 8, and 9. It is obvious from Figs. 5 and 8 that the probability of finding small particles near the large particles in the late stage is smaller than that for a random distribution with $d = 0$. Thus one must be careful in arriving at such a conclusion.

Figure 10 shows the radial distribution functions for various values of ϕ in the late stage. The radial distribution functions of a random distribution with $d = 0$ are also plotted for reference. The results shown are the averages of five different times in the late stage for $t > t_c$, where the values of t_c are listed in Table II. It is clear that the number density of particles is smaller at small distances than that of the random distributions with $d = 0$ for all cases. The qualitative features in the radial distribution function and the pair correlation functions are the same for all area fractions. Depletion zones do exist around the particles. In addition, the qualitative features of the real space correlation functions for two dimensions are the same as those in three dimensions [4].

The radial distribution and the pair correlation functions using the monopole and dipole approximations are compared in Figs. 3–6 and 10. Both of the approximations give the same qualitative results. However, we found small quantitative differences in the results. Note

that the differences between the particle size distribution functions using the monopole and dipole approximations are small, as will be shown later. Thus the differences in the radial distribution and pair correlation functions are mainly due to the different spatial correlations. The validity of the approximations will be discussed later.

B. Structure function

We characterize the spatial correlations of particles in Fourier space by the structure function. The structure function $\mathcal{S}(k,t)$ is defined as

$$\mathcal{S}(k,t) = \frac{\int \mathcal{S}(\mathbf{k},t)d\Omega}{\int d\Omega} = \left\langle \sum_{j=1}^{N}[\psi(kr_j)]^2 + \sum_{j=1}^{N}\sum_{\substack{j'=1 \\ j'\neq j}}^{N} \psi(r_j k)\psi(r_{j'}k)\exp(i\mathbf{k}\cdot\mathbf{x}_{jj'}) \right\rangle_{\Omega} \quad (k \neq 0), \tag{3.2}$$

where Ω is the angle in the k space, $\langle\,\rangle_\Omega$ is defined as the circular average, and $\psi(kr)$ is the form factor for a circle:

$$\psi(kr) = \frac{2\pi r}{k} J_1(kr). \tag{3.3}$$

Here $J_1(kr)$ is the Bessel function of the first kind and $\mathbf{x}_{jj'}$ is a vector locating the center of particle j' with its origin at the center of particle j. The first term in Eq. (3.2) is the scattering intensity from individual particles and the second term is the interference term. The pair correlation functions are basically the Fourier transforms of the second term. We define the structure function from individual particles, $\mathcal{S}_{\rm ip}(k,t)$, and the interference term $\mathcal{S}_{\rm int}(k,t)$ as

$$\mathcal{S}_{\rm ip}(k,t) = \sum_{j=1}^{N}[\psi(kr_j)]^2, \tag{3.4}$$

$$\mathcal{S}_{\rm int}(k,t) = \left\langle \sum_{j=1}^{N}\sum_{\substack{j'=1 \\ j'\neq j}}^{N} \psi(r_j k)\psi(r_{j'}k)\exp(i\mathbf{k}\cdot\mathbf{x}_{jj'}) \right\rangle_{\Omega}. \tag{3.5}$$

Thus

$$\mathcal{S}(k,t) = \mathcal{S}_{\rm ip}(k,t) + \mathcal{S}_{\rm int}(k,t). \tag{3.6}$$

If the system is in the scaling regime, the structure function obeys the scaling law:

$$\mathcal{S}(k,t) = \langle r\rangle^2 S(q), \tag{3.7}$$

where $q = k\langle r\rangle$ and $S(q)$ is the scaled structure function.

Figure 11 shows the scaled structure functions in the late stage at $\phi = 0.05$. The scaled structure functions are time independent in the late stage as expected. Note that at $t = 400$ the number of particles still remaining in the system is about 750. At this area fraction, the structure functions obtained by CTG and YEGG differ from the present results. Their structure functions are still time dependent at small wave numbers, and this may be due to an insufficiently large system size in their simulations.

Figure 12 shows a log-log plot of the structure functions shown in Fig. 11. The solid lines in the figure indicate the slopes of 4 and -3, respectively. In Fig. 11 the differences between the results using two different initial conditions are not noticeable. However, the different behaviors at very small wave numbers are clear in Fig. 12. The structure functions at a few of the smallest wave numbers still depend on time. It seems that the structure functions at very small wave numbers approach a single straight line of slope 4 as time increases. The results using the initial spatial distribution with $d = 2.5$ approach the asymptotic state faster. This q^4 dependence has been proposed theoretically for spinodal decomposition [20–22] and for coarsening [23,24]. It should be noted that we did not find any significant differences in the real space correlation functions in the late stage between the results using the initial spatial distributions with $d = 0$ and $d = 2.5$ beyond scatter in the data points. The structure function at small wave numbers may be very sensitive to spatial correlations. As mentioned earlier,

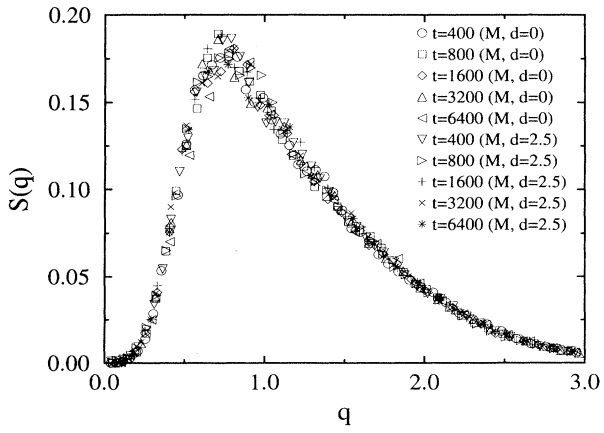

FIG. 11. The scaled structure functions in the late stage at $\phi = 0.05$.

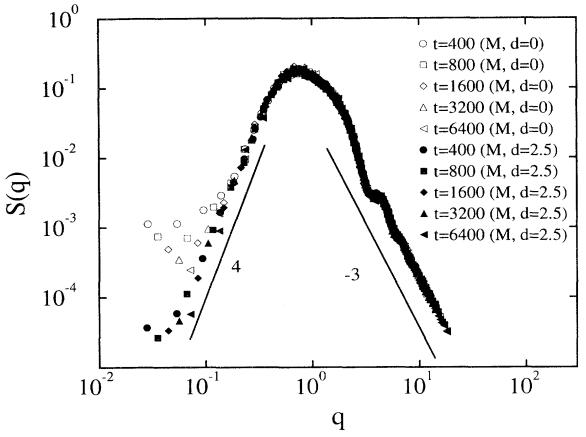

FIG. 12. A log-log plot of the scaled structure functions at $\phi = 0.05$. The solid lines indicate slopes of 4 and -3, respectively.

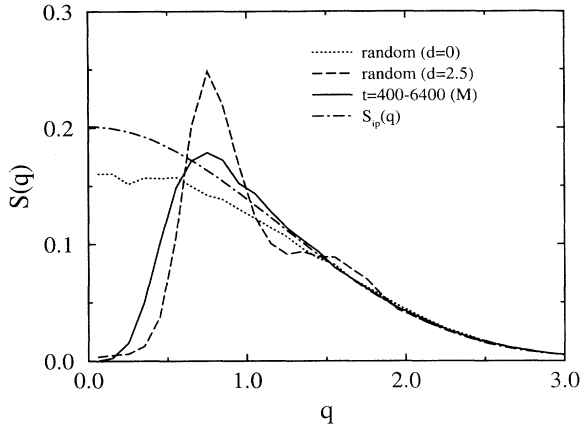

FIG. 13. Comparison of the scaled structure functions in the late stage and for random distributions at $\phi = 0.05$. The scattering intensity from individual particles $S_{ip}(q)$ is also plotted.

the interference term is the Fourier transform of the pair correlation functions. However, the relation between the q^4 dependence and the real space correlation functions is not clear for two and three dimensions. For the one-dimensional case, the structure function has a q^4 dependence at small wave numbers when the volume fraction is locally conserved and the particles are located at the center of the conserved area [22]. This is somewhat similar to what is found in the real space correlation functions. However, it is impossible to constrain all particles to satisfy the local area or volume fraction conservation condition in two and three dimensions.

At very large wave numbers, the structure function has the asymptotic form of $S(q) \sim q^{-3}$. This is Porod's law [25] which originates from the effect of the sharp interface. In the present simulations, the interface is always sharp so the structure function has the form of $S(q) \sim q^{-3}$ at all times. In the log-log plot shown in Fig. 12, oscillations at large q are clearly observed. These oscillations are related to the circular shape and the particle size distribution [22].

Figure 13 compares the scaled structure functions of random distributions with $d = 0$ and 2.5 with that in the late stage at $\phi = 0.05$. The late time results are the averages of the results with $d = 0$ and 2.5 shown in Fig. 11. The scaled structure function from individual particles, $S_{ip}(q)$, is also plotted in the figure for reference. The late time structure function smoothly approaches 0 as $q \to 0$. However, the structure functions for random distributions do not seem to approach 0 as $q \to 0$. Comparing the structure functions of random distributions and the late time results, it is clear that the structure function of a random distribution with $d = 2.5$ is closer to the late time results. This may be why the late time results using initial depletion zones approach the asymptotic results faster as shown in Fig. 12.

The scaled structure functions in the late stage using the monopole and dipole approximations at $\phi = 0.13$ and 0.2 are compared in Figs. 14 and 15, respectively. The results shown are the averages of five different times in the late stage. The real space correlation functions using the monopole and dipole approximations are slightly different as mentioned earlier. Those differences correspond to the differences in the structure functions shown in Figs. 14 and 15. At both values of ϕ the peaks of the structure functions using the dipole approximation are located at larger q than those using the monopole approximation. The differences are small at $\phi = 0.13$ but become larger at $\phi = 0.2$. The monopole approximation is a good approximation when the particles are well separated. As shown in Fig. 10, the separation distances between particles become smaller as ϕ increases. This is why the differences in the structure functions become larger as ϕ increases. The structure function obtained using the CH equation (CTG) [15] is also plotted in Fig. 15 for com-

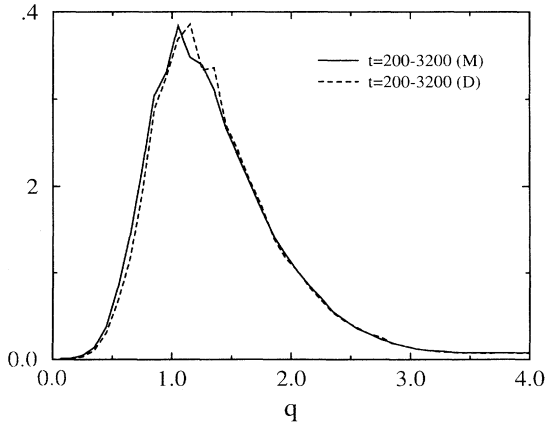

FIG. 14. The scaled structure functions at $\phi = 0.13$.

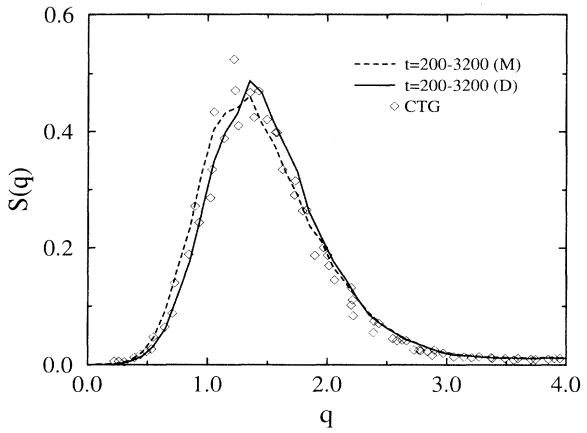

FIG. 15. The scaled structure functions at $\phi = 0.2$. The CTG [15] structure function is also plotted.

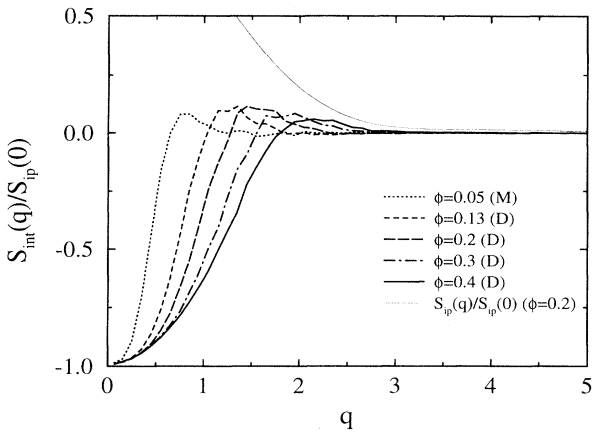

FIG. 17. The interference term normalized by $S_{\rm ip}(0)$ in the late stage for various ϕ.

parison. Note that $\phi = 0.21$ in their simulations. We found good agreement between the results of CTG and the present results using the dipole approximation.

Figure 16 shows the structure functions normalized by $S_{\rm ip}(0)$ for various values of ϕ. The normalized structure function from individual particles, $S_{\rm ip}(q)/S_{\rm ip}(0)$, for $\phi = 0.2$ is also plotted for reference. While $S_{\rm ip}(q)/S_{\rm ip}(0)$ depends on ϕ through the particle size distribution function, the effects of the size distributions are small in the present simulation since, as will be shown in Fig. 23, the differences in the size distribution functions are small. We can estimate the interference term by subtracting the scattering intensity from individual particles. The interference term is negative at small wave numbers, but becomes positive near the peak position. In order to see this behavior, the interference term normalized by $S_{\rm ip}(0)$ is plotted in Fig. 17. Using this normalization, the interference term approaches -1 as $q \to 0$ for all cases. The interference term asymptotically approaches 0 as q increases. However, we were not able to determine whether the asymptotic behavior is oscillatory or monotonic due to scatter in the data points. The quantity $S_{\rm ip}(q)/S_{\rm ip}(0)$ for $\phi = 0.2$ is also plotted in Fig. 17 for comparison. The interference terms are much smaller than $S_{\rm ip}(q)/S_{\rm ip}(0)$ at large wave numbers. Therefore we expect $S(q) \approx S_{\rm ip}(q)$ at large wave numbers. An asymptotic form of $\mathcal{S}_{\rm ip}(q)$ at large q is given by [26]

$$\mathcal{S}_{\rm ip}(k,t) \approx \sum_{j=1}^{N} \frac{8\pi r_j}{k^3} \cos^2\left(kr_j - \frac{3}{4}\pi\right) \approx \frac{4\pi N\langle r\rangle}{k^3}. \tag{3.8}$$

Thus

$$S_{\rm ip}(q) \approx \frac{4\pi N\langle r\rangle^2}{q^3} \tag{3.9}$$

at large q.

We define another normalization as

$$s(q) = \frac{1}{4\pi N\langle r\rangle^2} S(q). \tag{3.10}$$

Note that $N\langle r\rangle^2$ is a constant since $N \sim t^{-2/3}$. Using this normalization, we expect $s(q) = 1/q^3$ at large q. Figure 18 shows a log-log plot of the structure functions normalized by $4\pi N\langle r\rangle^2$. The solid lines in the figure indicate slopes of 4 and -3, respectively. Since the structure functions at a few of the smallest wave numbers do not scale well, as shown in Fig. 12, the results shown are the averages of the structure functions using the initial depletion zones at two latest times. The number of particles still remaining in the system is about 100–250 at these times. At large wave numbers all of the results collapse to a single straight line of slope -3 as expected from the definition. At small wave numbers the structure func-

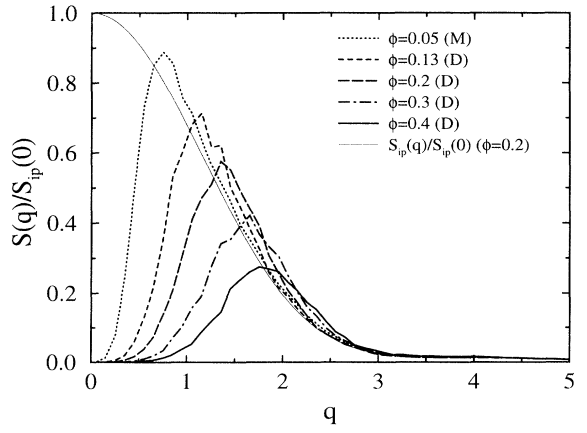

FIG. 16. The structure functions normalized by $S_{\rm ip}(0)$ in the late stage for various ϕ. The scattering intensity from individual particles $S_{\rm ip}(q)/S_{\rm ip}(0)$ is also plotted.

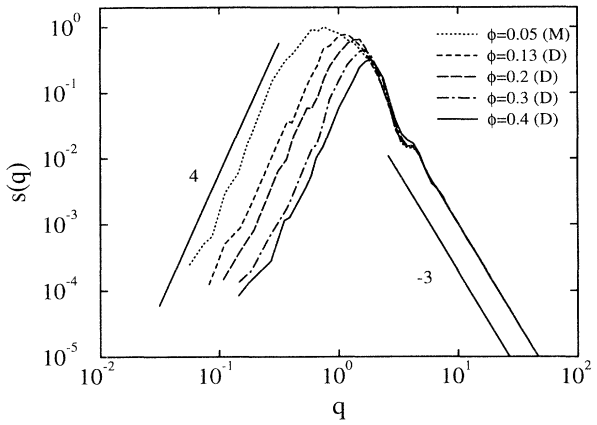

FIG. 18. A log-log plot of the structure functions normalized by $4\pi N\langle r\rangle$ for various ϕ. The solid lines indicate slopes of 4 and -3, respectively.

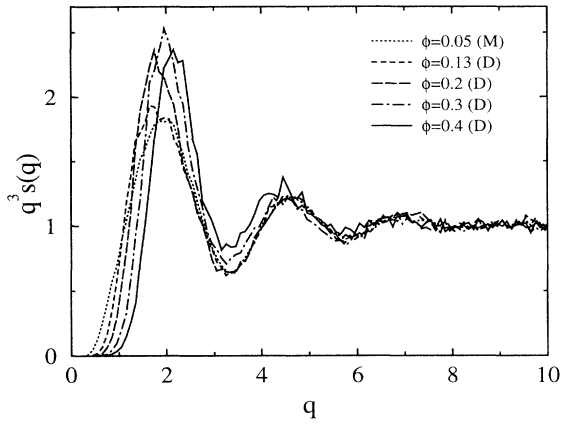

FIG. 19. A Porod plot of the structure functions normalized by $4\pi N\langle r\rangle$ for various ϕ.

tions seem to have a slope of 4 for all area fractions. The linear portion is over about 3/4 decade in q. Thus it is likely that the q^4 dependence is a generic behavior in late-stage coarsening.

We found that the magnitudes of the oscillations at large wave numbers are almost the same order except at $\phi = 0.4$. The magnitude of the oscillations depends on the width of the particle size distributions [22]. Since the differences in the size distribution are small in the present simulation, as will be shown later, the effects of the size distribution on the magnitude of the oscillations are small. At $\phi = 0.4$ the structure function near the first shoulder is higher than the others. This is because the interference term is still non-negligible at these wave numbers. If we plot $s_{\rm ip}(q)$ for various ϕ, all results almost collapse to a single curve. The position of the shoulder can be roughly estimated at the first zero of $\psi(k\langle r\rangle)$. Thus the position of the shoulder is given by $q \approx 3.8$ and does not depend on ϕ in the $s(q)$ versus q plot. However, the peak position of the interference term depends on ϕ, as shown in Fig. 17. Roughly speaking, the peak position of the interference term is inversely proportional to the peak position of the radial distribution function shown in Fig. 10. Since the peak position of the radial distribution functions moves toward smaller $x/\langle r\rangle$ as ϕ increases, the peak position of the interference term moves toward larger q as ϕ increases. Thus the interference term at the shoulder becomes non-negligible as ϕ increases.

A Porod plot, $q^3 s(q)$ versus q, is shown in Fig. 19. Using the normalization defined in Eq. (3.10), all of the results asymptotically approach 1 as q increases. The importance of the interference term can be clearly observed in this figure. At the first minimum, $q \approx 3.3$, the data points for $\phi = 0.05$, 0.13, and 0.2 are almost indistinguishable. The data points for $\phi = 0.4$ at the minimum are significantly higher than the others. As q increases, the differences become smaller since the interference term becomes negligible.

C. Particle size distribution function and rate constant

The particle size distribution function is obtained by averaging particle radii at five different times in the late stage. The particle size distribution function is normalized as

$$\int f(\rho)d\rho = 1, \tag{3.11}$$

where $\rho = r/\langle r\rangle$.

Figures 20–22 show the scaled particle size distribution functions at $\phi = 0.13$, 0.2, and 0.4, respectively. The present results and particle size distribution func-

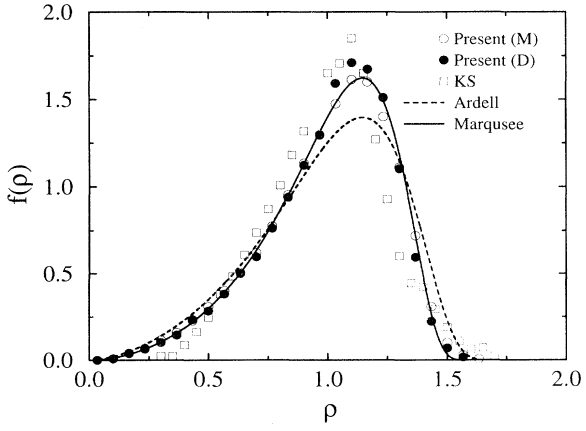

FIG. 20. Comparison of the particle size distribution functions in the late stage at $\phi = 0.13$. The experimental results by KS [19] and theoretical distribution functions obtained by Ardell [9] and Marqusee [5] are also plotted.

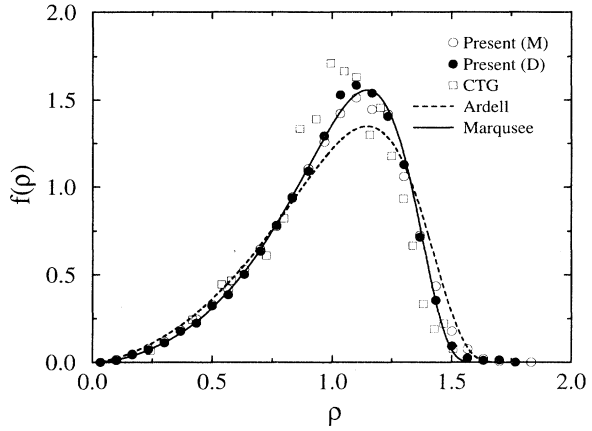

FIG. 21. Comparison of the particle size distribution functions in the late stage at $\phi = 0.2$. The results of numerical simulations by CTG [15] and theoretical distribution functions obtained by Ardell [9] and Marqusee [5] are also plotted.

tions determined by Ardell and Marqusee are plotted in the figures. In Figs. 20 and 22, the experimental results by KS are also plotted. The agreement between the experimental and present results is good at $\phi = 0.13$. At $\phi = 0.4$ the KS results are broader and the peak is lower than the present results. It should be noted that particles are no longer circular in experiments at this area fraction. Thus the differences may be caused by the circular shape of particles assumed in the simulations. The particle size distribution obtained by simulations using the CH equation (CTG) is also plotted in Fig. 21. It should be noted that $\phi = 0.21$ in their simulations. The CTG and present results agree well. As shown in Fig. 15, the CTG structure function agrees well with the present results. Thus we believe that the CH and present models give qualitatively the same results at $\phi = 0.2$. At all area fractions, the present results agree very well with the size distribution function obtained by Marqusee. In addition, the differences between the particle size distribution functions using the monopole and dipole approximations are very small, as shown in Figs. 20 and 21.

Figure 23 compares the particle size distributions at $\phi = 0.05$, 0.2, and 0.4. As ϕ increases, the particle size distribution function becomes broader. The results at $\phi = 0.13$ and 0.3 are not shown in the figure since the differences are not large. This is the main reason why the magnitudes of the oscillations in Fig. 18 are almost the same for all area fractions.

As shown in Fig. 2 and Table I, Eq. (3.1) holds in the late stage. The rate constant of the cubic growth law is determined by linear regression of $\langle r \rangle^3$ versus t in the late stage where $t > t_c$. Figure 24 compares the rate constants obtained by the present simulations with theoretical values obtained by Marqusee [5], Ardell [9], Yao *et al.* [11], and Zheng and Gunton [7], and simulation results by Yao *et al.* [11]. The present results agree well with the rate constants obtained by Marqusee. The other theories give much higher rate constants. As shown in Figs. 20–22, the size distribution functions of the present results also agree well with those obtained by Marqusee. Marqusee's theory is based on the modified Helmholtz equation for the average concentration c, which assumes a constant annihilation rate κ:

$$\nabla^2 c = \kappa^2 c. \tag{3.12}$$

κ is then determined in a self-consistent manner. We found that depletion zones exist around particles in the late stage, so the annihilation rate cannot be constant at all length scales. However, it is difficult to determine how the annihilation rate depends on location. The YEGG simulations give higher rate constants than those obtained from the present simulations. This may be because their systems do not reach an asymptotic state.

Finally, we discuss the validity of the present model. Simulations were performed using both monopole and dipole approximations at $\phi = 0.13$ and 0.2. The qualitative features of the spatial correlations using the monopole and dipole approximations are the same in both real and Fourier spaces. However, we observed small differences in the correlation functions. The differences are small at $\phi = 0.13$ but become larger at $\phi = 0.2$.

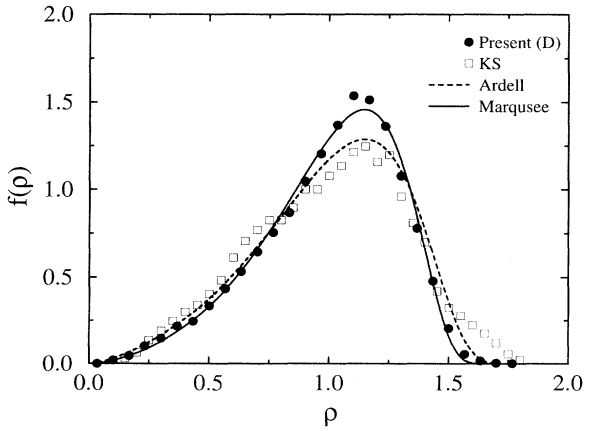

FIG. 22. Comparison of the particle size distribution functions in the late stage at $\phi = 0.4$. The experimental results by KS [19] and theoretical distribution functions by Ardell [9] and Marqusee [5] are also plotted.

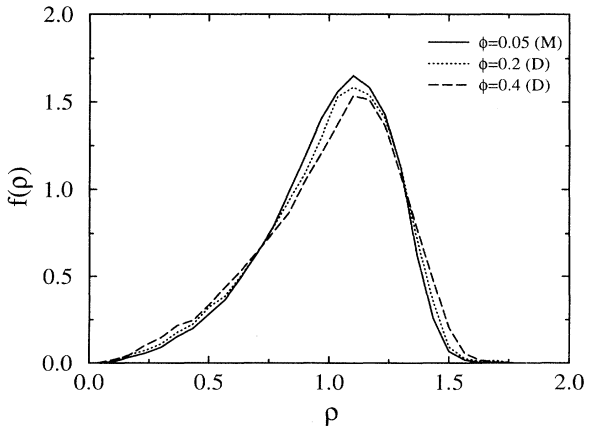

FIG. 23. The particle size distribution functions at various values of ϕ in the late stage.

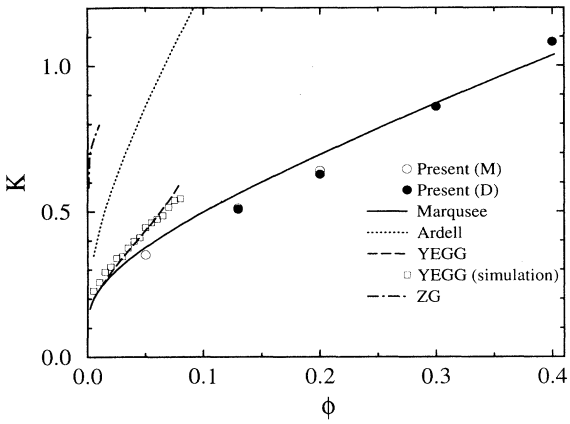

FIG. 24. Comparison of the rate constants in the late stage with those of other simulations and theories.

This is because separation distances between particles become smaller as ϕ increases. The differences in the particle size distributions and the rate constants using both of the approximations are small at both values of ϕ. Although the spatial correlations created using the monopole and dipole approximations are quantitatively different, the effects of these differences on the kinetics of coarsening is very small. Since the differences are small at $\phi = 0.13$, we can conclude that the monopole approximation is a good approximation at this area fraction. While the monopole approximation is not a poor approximation at $\phi = 0.2$, the dipole approximation does give an improved result. In addition, the present results agree well with the experimental results at $\phi = 0.13$. We also found good agreement between the simulation results using the CH equation and the present model at $\phi = 0.2$. Thus we may conclude that the late-stage coarsening process is well demonstrated in the present simulations. We cannot argue about the validity of the dipole approximation from the present simulation. The differences in the particle size distribution between the experimental and present results are not small at $\phi = 0.4$. These differences may be due to the circular shape of particles assumed in the present simulations. Simulations performed without the shape restriction can be used to assess the validity of the dipole approximation. This work, using the fast multipole method, is currently in progress.

IV. CONCLUSIONS

We have performed numerical simulations of late-stage coarsening using the monopole and dipole approximations of the steady state diffusion equation at various area fractions. The cubic growth law of the average radius was confirmed for all area fractions. Thus the LSW scaling law is also applicable in two dimensions.

It is well known that the scaled particle size distribution function evolves to a unique distribution at a given area fraction which seems to be an attractor in the late stage. We found that the scaled particle correlation functions using different initial spatial distributions also evolve to unique time-independent forms. The scaled spatial correlation functions also have attractors in the late stage. The important feature in the real space correlation functions is that depletion zones exist around particles. The number density of particles in the vicinity of a particle is smaller than that of a random spatial distribution. In addition, the qualitative features of the late-stage spatial correlations in two dimensions are the same as those in three dimensions.

The structure function seems to have an asymptotic form of $S(q) \sim q^4$ at small wave numbers for all area fractions. The relation between this behavior and the real space correlation functions is still unclear. At large wave numbers we found oscillations around the Porod tail of q^{-3}. The magnitudes of the oscillations are comparable for all area fractions except at $\phi = 0.4$ since the differences in the size distribution functions are small in the present simulations. For $\phi \leq 0.3$ the oscillatory behavior can be described by the scattering intensity from individual particles since the interference term is small at these wave numbers. However, the interference term is not negligible at $\phi = 0.4$.

The differences between the results using the monopole and dipole approximations at $\phi = 0.13$ are small. Thus the monopole approximation is a good approximation at this area fraction. For higher area fractions, the dipole terms should be included. Unfortunately, we cannot determine the validity of the dipole approximation from the present simulations. Simulations in which the particles are allowed to change their shapes must be performed to determine the validity of the dipole approximation.

Although the present model is simple, we found good agreement with experiments and simulations using the CH equation. Thus we believe that the qualitative features of the late-stage coarsening process are well described in the present simulations.

ACKNOWLEDGMENTS

We would like to thank Professor P. W. Voorhees for helpful comments. This work was supported by DOE Grant No. DE-FG03-89ER-25073.

APPENDIX

To perform the integral in Eq. (2.6) we expand $g(\mathbf{p},\mathbf{q})$ in powers of the separation distance. When the field point is on particle j and the integration point is on particle k, $g(\mathbf{p},\mathbf{q})$ is given by

$$g(\mathbf{p},\mathbf{q}) = \ln|\mathbf{d}_{jk} - \mathbf{r}_j + \mathbf{r}_k|, \tag{A1}$$

where $\mathbf{d}_{jk}$ is a vector emanating from the center of particle j to the center of particle k. Expanding Eq. (A1) in powers of r/d, we obtain

$$g(\mathbf{p},\mathbf{q}) = \ln d_{jk} - \sum_{n=1}^{\infty}\sum_{m=0}^{n} \frac{(-1)^m}{n}\binom{n}{m}\frac{r_j^{n-m} r_k^m}{d_{jk}^n} \times \cos[-n\theta_{d_{jk}} + (n-m)\theta_{r_j} + m\theta_{r_k}], \tag{A2}$$

where r_j, r_k, d_{jk} are norms of the vectors $\mathbf{r}_j$, $\mathbf{r}_k$, $\mathbf{d}_{jk}$, respectively. Performing the integral in Eq. (2.6) using Eq. (A2),

$$\int_{S_k} \sigma(\mathbf{q}) g(\mathbf{p},\mathbf{q}) d\mathbf{q} = \pi r_k A_0^{(k)} \ln d_{jk} - \sum_{n=1}^{\infty} \sum_{m=0}^{n} \frac{(-1)^m \pi}{n} \binom{n}{m} \frac{r_j^{n-m} r_k^{m+1}}{d_{jk}^n} \Big\{ A_m^{(k)} \cos[n\theta_{d_{jk}} - (n-m)\theta_{r_j}] + B_m^{(k)} \sin[n\theta_{d_{jk}} - (n-m)\theta_{r_j}] \Big\} \quad \text{for } \mathbf{p} \text{ on } S_j, \ \mathbf{q} \text{ on } S_k. \tag{A3}$$

When both the integration point and the field point are located on the same particle, $g(\mathbf{p},\mathbf{q})$ is singular and cannot be expanded. However, the single layer potential due to particle j for all $\mathbf{p}$ except on S_j is given by

$$\int_{S_j} \sigma(\mathbf{q}) g(\mathbf{p},\mathbf{q}) d\mathbf{q} = \begin{cases} \pi A_0^{(j)} r_j \ln r_j - \sum_{n=1}^{\infty} \left[A_n^{(j)} \cos(n\theta_p) + B_n^{(j)} \sin(n\theta_p) \right] \frac{\pi}{n} \frac{p^n}{r_j^{n-1}} & \text{for } \mathbf{p} \text{ inside } S_j \quad \text{(A4a)} \\ \pi A_0^{(j)} r_j \ln p - \sum_{n=1}^{\infty} \left[A_n^{(j)} \cos(n\theta_p) + B_n^{(j)} \sin(n\theta_p) \right] \frac{\pi}{n} \frac{r_j^{n+1}}{p^n} & \text{for } \mathbf{p} \text{ outside } S_j. \quad \text{(A4b)} \end{cases}$$

Since the single layer potential is continuous across the boundary, the integral on S_j can be evaluated by setting $p = r_j$ in Eq. (A4),

$$\int_{S_j} \sigma(\mathbf{q}) g(\mathbf{p},\mathbf{q}) d\mathbf{q} = \pi A_0^{(j)} r_j \ln r_j - \sum_{n=1}^{\infty} \frac{\pi r_j}{n} \left[A_n^{(j)} \cos(n\theta_p) + B_n^{(j)} \sin(n\theta_p) \right] \quad \text{for } \mathbf{p} \text{ on } S_j. \tag{A5}$$

[1] J. W. Cahn and J. E. Hilliard, J. Chem. Phys. **28**, 258 (1958).
[2] I. M. Lifshitz and V. V. Slyozov, J. Phys. Chem. Solids **19**, 35 (1961).
[3] C. Wagner, Z. Elektrochem. **65**, 581 (1961).
[4] N. Akaiwa and P. W. Voorhees, Phys. Rev. E **49**, 3860 (1994).
[5] J. A. Marqusee, J. Chem. Phys. **81**, 976 (1984).
[6] H. Hayakawa and F. Family, Physica A **163**, 491 (1990).
[7] Q. Zheng and J. D. Gunton, Phys. Rev. A **39**, 4848 (1989).
[8] M. Marder, Phys. Rev. A **36**, 858 (1987).
[9] A. J. Ardell, Phys. Rev. B **41**, 2554 (1990).
[10] A. J. Ardell, Acta Metall. **20**, 61 (1972).
[11] J. H. Yao, K. R. Elder, H. Guo, and M. Grant, Phys. Rev. B **47**, 14110 (1993).
[12] P. W. Voorhees, G. B. McFadden, R. F. Boisvert, and D. I. Meiron, Acta Metall. **36**, 207 (1988).
[13] T. Imaeda and K. Kawasaki, Physica A **164**, 335 (1990).
[14] T. M. Rogers and R. C. Desai, Phys. Rev. B **39**, 11956 (1989).
[15] A. Chakrabarti, R. Toral, and J. D. Gunton, Phys. Rev. E **47**, 3025 (1993).
[16] A. M. Lacasta, J. M. Sancho, A. Hernández-Machado, and R. Toral, Phys. Rev. B **48**, 6854 (1993).
[17] T. Küpper and N. Masbaum, Acta Metall. **42**, 1847 (1994).
[18] M. Tokuyama and K. Kawasaki, Physica A **123**, 386 (1984).
[19] O. Krichevsky and J. Stavans, Phys. Rev. Lett. **70**, 1473 (1993).
[20] H. Furukawa, J. Phys. Soc. Jpn. **58**, 216 (1989).
[21] C. Yeung, Phys. Rev. Lett. **61**, 1135 (1988).
[22] P. Fratzl, J. L. Lebowitz, O. Penrose, and J. Amar, Phys. Rev. B **44**, 4794 (1991).
[23] M. Tokuyama and Y. Enomoto, Phys. Rev. E **47**, 1156 (1993).
[24] G. F. Mazenko and R. A. Wickham (unpublished).
[25] G. Porod, in *Small Angle X-ray Scattering*, edited by O. Glatter and O. Kratky (Academic Press, London, 1983), pp. 17–51.
[26] H. Tomita, Prog. Theor. Phys. **75**, 482 (1986).